AJG

Article

Wavelets for Non-metric Camera Self-calibration

Jun-Fu Ye*[1], Jaan-Rong Tsay[2], and Dieter Fritsch[3]

[1,2]Department of Geomatics, National Cheng Kung University, No. 1, Daxue Rd., East Dist., Tainan City 701401, Taiwan (R.O.C.) [1]<junfu.ye@gmail.com>, [2]<tsayjr@ncku.edu.tw>

[3]Institute for Photogrammetry and Geoinformatics, University of Stuttgart, Geschwister-Scholl-Str. 24D, 70174 Stuttgart, Germany. <dieter.fritsch@ifp.uni-stuttgart.de>

*Corresponding author: J-F Ye, Email: <junfu.ye@gmail.com>

Received: July 18, 2026; Accepted: September 13, 2026; Published: September 22, 2026

ABSTRACT

This study evaluates the developed Wavelet Additional Parameter (WAP) models for non-metric camera self-calibration under diverse control and navigation constraints. Empirical results from the 24 test cases demonstrate that the developed WAPs achieve RMSD(XY) and RMSD(Z) reductions of 78.8%–86.3% and 83.6%–95.6%, respectively, relative to the uncompensated cases. Furthermore, these WAPs successfully mitigate lens distortions without underfitting through their spatial localization and orthogonality. Under the Type 2 configuration (sparse GCPs supplemented with navigation data), the developed models exhibit superior internal consistency, outperforming the traditional BINGO polynomial model by 33.3%–38.4% and 30.7%–36.0% in terms of tie-point *a posteriori* precisions in the RMS($\hat{\sigma}_{XY}$) and RMS($\hat{\sigma}_{Z}$), respectively. By leveraging mathematically orthogonal wavelet bases and an adaptive screening workflow to prevent overparameterization, this approach ensures high numerical stability and effectively bridges the gap between low-cost sensors and high-precision UAV-based aerial surveying.

Keywords: Bundle adjustment, Wavelet Additional Parameters (WAPs), Camera self-calibration, Systematic errors

1. INTRODUCTION

Aimé Laussedat, the father of photogrammetry, pointed out in his book (1898, 373–74) that the early development of photogrammetry was difficult, partly due to image distortion caused by lens imperfections. Following the invention of powered flight in the early 20th century, aerial photography adopted fixed-wing aircraft as a platform. The correction of geometric image distortions gained significant practical attention during World War I, driven by militaries' recognition of the strategic value of aircraft for reconnaissance and mapping. In the early 20th century, Deville pioneered visual calibration by instituting collimator-based methods for both terrestrial and early aerial camera characterization. Subsequently, the National Bureau of Standards (NBS) standardized calibration procedures by implementing photographic methods utilizing multi-collimator arrays. In contrast, European manufacturers such as Wild Heerbrugg and Zeiss favored the goniometer method, an alternative visual approach that determined geometric constants by reversing the optical path (Clarke and Fryer 1998).

Although laboratory calibration using multi-collimators or goniometers establishes the foundation for optical compensation, discrepancies between controlled laboratory conditions and actual operational environments, such as variations in temperature and atmospheric pressure, can still cause significant changes in lens distortion. To address these physical limitations, geometric camera calibration transitioned from analog optical compensation to analytical photogrammetry. In the 1950s, Brown had already used the precisely known celestial positions to calibrate ballistic cameras, thereby reducing the influence of environmental factors through mathematical modeling. However, both stellar and laboratory methods have a fundamental limitation: they cannot simulate in situ dynamic operational environments (Brown 1968).

To overcome the limitations of static environments, two complementary pathways emerged in the early 1970s for calibrating imaging systems under active operational conditions: Merchant (1972) extended controlled experimentation to outdoor test fields with geodetic control, while Brown (1971) established the principles of on-the-job self-calibration by integrating additional parameters (APs) directly into bundle adjustment. Within this backdrop, the International Society for Photogrammetry (ISP) instituted specialized Working Groups dedicated to standardizing camera calibration and systematic error compensation. Simultaneously, researchers developed various AP models based on physical phenomena or mathematical polynomials to calibrate analog single-head cameras using self-calibrating bundle adjustment.

Brown (1971) applied his seminal physical AP model to close-range camera calibration using the analytical plumb-line method. Based on the theory of optical ray tracing, his model mathematically reformulated the radial distortion model of Magill (1955) and the decentering distortion model of Conrady (1919) to meet the requirements of close-range photogrammetry. Furthermore, Brown (1976) integrated empirical polynomial terms to compensate for film deformation and platen unflatness, thereby extending his model to aerial applications within the self-calibrating bundle adjustment framework.

Unlike physical AP models, which require explicit geometric or optical interpretations, mathematical AP models rely on orthogonal polynomials to fit and compensate for systematic errors. Concurrently, Ebner (1976) introduced a landmark 12-parameter mathematical model based on orthogonal second-order bivariate algebraic polynomials, thereby avoiding the high parameter correlations inherent in Brown's model. Building upon these concepts, Grün (1978) expanded Ebner's model to 44 parameters using orthogonal fourth-order bivariate algebraic polynomials to further compensate for systematic errors. Fritsch (2015, 2017) demonstrated that the mathematical foundation of photogrammetric self-calibration traces back to the 19th-century Weierstrass Theorem, thus framing the entire methodology as a problem of functional approximation.

The experimental results of the ISP(RS) Working Group III/3 demonstrated that both physical and mathematical AP models are equally effective at compensating for systematic image errors and yield similar results. Ackermann (1981) reviewed the theoretical status and practical conditions for safe AP application, emphasizing that the determinability and reliability of these parameters depend heavily on rigorous statistical screening and network geometry, and maintaining that future adjustments should treat systematic image errors as a stochastic process. However, in minimally constrained networks, Fraser (1982) demonstrated that increasing the order of APs can degrade object-space accuracy. This over-parameterization induces projective compensation, causing the model to overfit the image plane.

According to Fraser (1997), high-resolution digital cameras utilizing digital charge-coupled device (CCD) sensors had, by that time, almost replaced analog film cameras in image-acquisition workflows for close-range photogrammetric applications. The four primary sources of departures from collinearity in digital cameras are characterized as radial lens distortion, decentering distortion, out-of-plane distortion, and in-plane distortion. Compared with film cameras, CCD sensors exhibit highly stable and rigid geometric errors, thereby rendering them well-suited for analytical self-calibration. Consequently, the classic Brown AP model and its extended formulations remain the preferred methods for camera calibration in the digital age.

Cramer (2009) delivered the final report of the European Spatial Data Research (EuroSDR) network, completed in 2007, on the geometric calibration and validation of the ADS40, DMC, and UCD digital aerial cameras. The empirical results confirmed that introducing APs for self-calibration and setting a priori observation weights are crucial for achieving sub-pixel-level geometric accuracy. However, the study also noted that the choice of APs depends on the sensor's geometry. The standard Brown model is sufficient for calibrating the ADS40 line-scanning system. Multi-head frame systems like the DMC and UCD require extended models or the Grün model because the standard or Ebner models appear insufficient to compensate for systematic errors. Fritsch (2015) noted that while conventional APs have retained utility in the digital era, they might fail to accommodate the distinctive geometric features of modern aerial cameras, such as push-broom scanning, multi-head configurations, virtual image composition, and diverse image formats.

Tang et al. (2012a) proposed a new family of self-calibration APs based on orthogonal Legendre polynomials for the calibration of digital aerial frame camera systems. While this model successfully generalizes Ebner's and Grün's models, it still retains the inherent limitations of algebraic polynomial APs. These limitations include high parameter correlation and a compromise of mathematical rigor in function approximation to suppress it (Tang et al. 2012b).

To address these deficiencies, Tang et al. (2012b) introduced alternative self-calibration APs based on bivariate Fourier series for calibrating aerial frame camera systems. Grounded in rigorous mathematical foundations, the Fourier-based approach requires fewer parameters to compensate for systematic distortions, and practical tests confirm its high efficiency.

Despite these theoretical advancements, the diversification of modern imaging platforms introduces new challenges, as photogrammetric applications increasingly employ non-metric cameras. Unlike highly stable metric cameras, these non-metric devices may exhibit irregular or localized distortion patterns. The periodic nature of the Fourier series renders this method incapable of effectively compensating for non-stationary distortion signals. Consequently, attempting to model such non-stationary components with global Fourier APs can lead to the Gibbs phenomenon, particularly near image boundaries.

To overcome these methodological constraints, Ye et al. (2024) developed a novel series of self-calibration models based on orthogonal wavelets, called wavelet APs (WAPs), capable of compensating for both stationary and non-stationary systematic image distortions. That paper primarily evaluated the empirical performance of WAPs on aerial metric camera systems. To extend that research, this paper investigates the applicability and performance of WAPs on non-metric cameras through empirical testing.

The remaining sections of this paper present the research framework as follows: Section 2 presents the proposed WAP models for self-calibration; Section 3 introduces the non-metric camera test dataset; Section 4 evaluates and discusses the experimental results; and Section 5 summarizes our findings and contributions.

2. WAP MODELS FOR SELF-CALIBRATION

Analytical self-calibration via bundle adjustment is a mature methodology for camera self-calibration in photogrammetry and computer vision. The geometric foundation of this framework relies on the classic collinearity equations (Wolf et al. 2014, 268–69) as given by (1):

$$\begin{aligned} x &= x_0 - c\frac{m_{11}(X-X_0)+m_{12}(Y-Y_0)+m_{13}(Z-Z_0)}{m_{31}(X-X_0)+m_{32}(Y-Y_0)+m_{33}(Z-Z_0)} + \Delta x + \varepsilon_x \\ y &= y_0 - c\frac{m_{21}(X-X_0)+m_{22}(Y-Y_0)+m_{23}(Z-Z_0)}{m_{31}(X-X_0)+m_{32}(Y-Y_0)+m_{33}(Z-Z_0)} + \Delta y + \varepsilon_y \end{aligned} \tag{1}$$

where *x* and *y* are the measured photo coordinates of an image point of interest; x_0 and y_0 are the photo coordinates of the principal point; *c* is the principal distance of the camera; *m's* are the elements of the orthogonal rotation matrix *M* derived from the sequential rotation angles ω, ϕ, and κ, defining the spatial orientation of the photo at the moment of exposure; X_0, Y_0, and Z_0 are the object space coordinates of the camera's perspective center at the moment of exposure; *X*, *Y*, and *Z* are the object space coordinates of the target point of interest; Δx and Δy are the systematic error components expressed by the WAPs adopted in this paper to model geometric image distortions; and ε_x and ε_y are the random error components associated with *x* and *y*, respectively.

Compared to Fourier series, which relies on globally unattenuated sinusoids, well-constructed wavelet bases in the Hilbert space $L^2(\mathbb{R})$ exhibit time-frequency localization, thereby offering a more flexible framework for the adaptive approximation of unknown signals. However, unlike Fourier series using fixed kernel functions, the approximation efficiency of wavelet methods depends on the mathematical characteristics of the chosen wavelet basis. Since wavelet bases differ significantly in properties such as orthogonality, compact support, symmetry, and vanishing moments, selecting an appropriate basis is a critical step in achieving optimal signal representation. In this study, orthogonality is the primary criterion for approximating unknown signals, as it guarantees a non-redundant representation.

Therefore, we utilize four classic orthogonal wavelet families to construct various sets of WAPs: the asymmetric Daubechies (ADB), least asymmetric Daubechies (LADB), Meyer, and Battle-Lemarié (BL) wavelets. The ADB and LADB wavelets provide compact support and controllable vanishing moments for localized feature extraction, yet they present varying degrees of asymmetry. In contrast, when strict symmetry is critical, the frequency-domain compactly supported Meyer wavelets and the spline-based BL wavelets offer alternative selections; however, these latter two families lack compact support in the time domain (Daubechies 1992).

Under Mallat's (1989) multiresolution analysis (MRA) framework, the approximation of the unknown systematic signal constitutes an orthogonal projection onto a closed subspace V_j of the Hilbert space $L^2(\mathbb{R})$ at a given scale j. The sequence of closed subspaces $\{V_j\}_{j\in\mathbb{Z}}$ satisfies the following nested structure parameterized by the resolution scale:

$$\{0\} \subset \cdots \subset V_{-1} \subset V_0 \subset V_1 \subset \cdots \subset L^2(\mathbb{R}) \quad (2)$$

where a higher j value yields a finer-resolution representation of the unknown systematic image distortion.

According to MRA, the scaling functions $\{\phi_{j,k}\}_{k\in\mathbb{Z}}$, derived from the scaling and translation of the father wavelet ϕ, form an orthonormal basis for the subspace V_j at any given scale j, where k is an integer translation parameter. A linear combination of these basis functions constitutes the best approximation function $A_j f$ with minimum error energy. Concurrently, the wavelet functions $\{\psi_{j,k}\}_{k\in\mathbb{Z}}$, derived from the scaling and translation of the mother wavelet ψ, form an orthonormal basis for the subspace W_j. Their linear combination yields the detail function $D_j f$ with localized high-frequency energy.

The direct sum of these two orthogonal subspaces, $V_{j+1} = V_j \oplus W_j$, describes a finer-resolution representation of the unknown systematic signal. Specifically, the sum of the approximation and detail components yields the best approximation function of f in V_{j+1}:

$$A_{j+1}f(t) = A_j f(t) + D_j f(t) \quad (3)$$

where

$$A_j f(t) = \textstyle\sum_k \langle f, \phi_{j,k}\rangle \phi_{j,k}(t) \quad (4)$$

$$D_j f(t) = \textstyle\sum_k \langle f, \psi_{j,k}\rangle \psi_{j,k}(t) \quad (5)$$

with $\langle\cdot,\cdot\rangle$ denoting the standard inner product in the Hilbert space $L^2(\mathbb{R})$.

To approximate unknown systematic geometric distortions of two-dimensional (2D) images, we generalize Mallat’s (1989) 2D multiresolution framework within the Hilbert space $L^2(\mathbb{R}^2)$. The tensor product of two closed univariate subspaces, $V_{j_x+1} \otimes V_{j_y+1}$, defines the 2D multiresolution space $\mathbf{V}_{j_x+1,j_y+1}$. This anisotropic formulation yields the following generalized 2D orthonormal basis functions.

$$\Phi_{j_x,j_y;k_x,k_y}(x_w, y_w) = \phi_{j_x,k_x}(x_w)\phi_{j_y,k_y}(y_w) \quad (6)$$

$$\Psi^h_{j_x,j_y;k_x,k_y}(x_w, y_w) = \phi_{j_x,k_x}(x_w)\psi_{j_y,k_y}(y_w) \quad (7)$$

$$\Psi^v_{j_x,j_y;k_x,k_y}(x_w, y_w) = \psi_{j_x,k_x}(x_w)\phi_{j_y,k_y}(y_w) \quad (8)$$

$$\Psi^d_{j_x,j_y;k_x,k_y}(x_w, y_w) = \psi_{j_x,k_x}(x_w)\psi_{j_y,k_y}(y_w) \quad (9)$$

Here, j_x and j_y denote the resolution scales along the x_w- and y_w-axes, respectively, while k_x and k_y represent the corresponding integer translations. The superscripts *h*, *v*, and *d* denote the horizontal, vertical, and diagonal detail components, respectively, which capture the directional features across the decoupled scales. Finally, this formulation reduces to Mallat's standard isotropic model as a special case when $j_x = j_y = j$.

We establish a direct correspondence between the functional coordinates (x_w, y_w) of the 2D wavelet bases and the photo coordinates (*x*, *y*) of the 2D images to model the underlying systematic image distortions. Specifically, a regular grid divides the 2D image domain based on the image dimensions (*W*, *H*) and a predefined number of grid partitions, $G_x \times G_y$. This grid configuration simultaneously dictates both the resolution scales and the translation steps of the wavelet bases. Consequently, the mapping function transforms the photo coordinates into the normalized wavelet domain via:

$$x_w = xG_x/W\,, y_w = yG_y/H \quad (10)$$

Grounded in approximation and wavelet theories, two distinct formulations characterize the systematic error components, *Δx* and *Δy*. The first formulation models image distortion within the subspace $\mathbf{V}_{j_x,j_y}$ as a linear combination of 2D scaling functions shown in Equation (6), thereby subsuming all detail components from lower resolution levels. Alternatively, the second formulation spans the higher-resolution subspace $\mathbf{V}_{j_x+1,j_y+1}$ via a linear combination of Equations (6) to (9), thereby incorporating directional details between adjacent resolution scales. Specifically, we define the first approach as:

$$\begin{aligned} \Delta x(x,y) &= \textstyle\sum_{k_y=LBy}^{UBy} \sum_{k_x=LBx}^{UBx} a_{j_x,j_y;k_x,k_y} \Phi_{j_x,j_y;k_x,k_y}(x_w, y_w) \\ \Delta y(x,y) &= \textstyle\sum_{k_y=LBy}^{UBy} \sum_{k_x=LBx}^{UBx} a'_{j_x,j_y;k_x,k_y} \Phi_{j_x,j_y;k_x,k_y}(x_w, y_w) \end{aligned} \quad (11)$$

where $a_{j_x,j_y;k_x,k_y}$ and $a'_{j_x,j_y;k_x,k_y}$ denote the unknown WAPs. The support of the selected wavelet bases governs the integer translation bounds, [*LBx*, *UBx*] and [*LBy*, *UBy*], for k_x and k_y along the x_w- and y_w-axes, respectively. While the compact support of ADB and LADB wavelets directly dictates these limits, Meyer and BL wavelets require specific computational precision thresholds to truncate the expansion when the basis functions decay to negligible magnitudes. Subsequently, the variance-covariance matrix derived from bundle adjustment enables statistical significance and correlation tests to screen individual WAPs, adopting threshold criteria established in the classic BINGO software manual (Kruck 2021). By eliminating redundant or insignificant WAPs and tightening the translation bounds, the proposed approach yields an optimized distortion representation. Also, this study employed the unified approach to least squares adjustment (Mikhail and Ackermann 1976).

3. TESTS ON A NON-METRIC CAMERA

The image dataset was acquired at the Nangang Geometric Calibration Field, an official calibration site maintained by the National Land Surveying and Mapping Center (NLSC), Ministry of the Interior, Taiwan. A total of 39 geometric calibration marks, remeasured annually via high-precision global navigation satellite system (GNSS) observations, serve as ground control points (GCPs) and independent check points (CHKs) for the self-calibration bundle adjustment. According to the official report (NLSC 2015), the combined standard uncertainties of the ground coordinates for these geometric calibration marks are approximately 16.7 mm and 28.9 mm in the horizontal (XY) and vertical (Z) components, respectively.

The aerial photography mission was executed on September 2, 2020, by GEOSAT Aerospace & Technology Inc. using a rotary-wing uncrewed aerial vehicle (UAV). The imaging system consisted of a Sony ILCE-7M3 digital camera equipped with a ZEISS Loxia 2.8/21 prime lens. According to the manufacturer's specifications, the camera sensor features a nominal pixel size of approximately 5.9 μm by 5.9 μm with an image format of 6000 pixels by 4000 pixels.

We selected a subset of 28 vertical aerial images for self-calibration studies. These images comprise four parallel east-west flight strips, with each strip containing seven sequential frames. The flight configuration maintained a forward lap of approximately 75% and a side lap of approximately 60%. Flying at an average altitude of 215 m above ground level (AGL), the system achieved a ground sampling distance (GSD) of approximately 6.1 cm and an average image scale of 1:10,300.

This study evaluates the performance of the WAP models by comparing them with traditional AP models implemented in the commercial BINGO software. We integrated a strip-dependent shift-and-drift parameter model into the bundle adjustment framework to compensate for systematic errors in the kinematic trajectory data. The mathematical compensation applied to the GNSS/inertial measurement unit (IMU) trajectory observations within each strip is formulated as follows:

$$P = P_0 + D_0 + D_1 \Delta t + D_2 \Delta t^2 \quad (12)$$

where P is the GNSS/IMU trajectory observation data; P_0 is the corresponding trajectory coordinate and attitude derived from the exterior orientation parameters (EOPs) of each image, defined by X_0, Y_0, Z_0, ω, ϕ, and κ; Δt is the elapsed time interval within the specific flight strip; D_0 is the constant shift coefficient; and D_1 and D_2 are the first- and second-order drift coefficients, respectively. As with the WAP approach, we implemented statistical significance and correlation tests to screen individual shift-and-drift parameters, thereby achieving an optimized parameterization.

Conversely, the comparative cases processed in BINGO relied on its built-in mathematical formulations rather than our customized model. The software utilized GNSS shift/drift parameters and IMU misalignment values to account for trajectory biases and boresight misalignments.

All test cases employed Baarda's data snooping method (Baarda, 1968) for outlier detection. This approach systematically excludes any image coordinate observation whose absolute standardized residual exceeds a critical value of 3.0. For cases that included APs or GNSS/IMU shift-and-drift parameters, the workflow further integrated statistical screening via significance and correlation tests at each iteration. For the cases incorporating the proposed WAPs described in Section 2, we define a uniform 9 × 6 grid network for each image to match the 3:2 aspect ratio of the image frame. Although the algorithm supports arbitrary grid dimensions, optimization of this parameterization configuration is left for future work.

In all test cases, the average image point density on the image plane ranges from 3.2 to 3.9 points/mm^2. Figure 1 illustrates the spatial distribution for the case with the minimum point density. Mapping all image points onto the designated 9 × 6 grid network results in 10–103 points per cell, ensuring sufficient measurement redundancy across the entire image frame.

Among the four proposed families of WAPs, those based on ADB, BL, and LADB wavelets are each parameterized by their respective orders. In theory, distinct sets of WAPs can be established across any order of these wavelet bases. For experimental feasibility, however, this investigation restricts its current scope to the fourth-order case as a demonstrative example, denoted herein as ADB4, BL4, and LADB4, respectively.

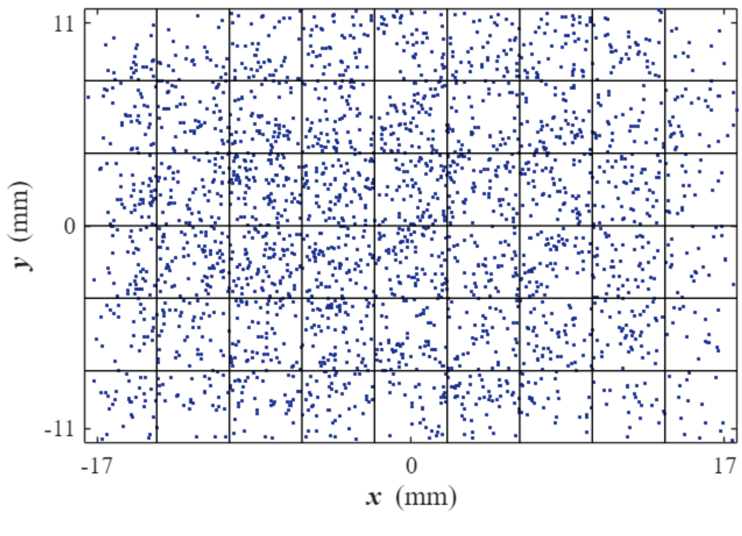

Figure 1. Spatial distribution of the retained tie points after outlier detection for the minimum-density case (3.2 points/mm^2), overlaid on the designated 9 × 6 grid network.

To evaluate their performance, we conducted 24 test cases by combining four testing scenarios with six AP models. Specifically, we combined two reference point configurations and two trajectory constraints to establish four testing scenarios: (1) a low-density configuration (15 GCPs and 24 CHKs) without GNSS/IMU as Type 1; (2) a low-density configuration with GNSS/IMU as Type 2; (3) a high-density configuration (27 GCPs and 12 CHKs) without GNSS/IMU as Type 3; and (4) a high-density configuration with GNSS/IMU as Type 4. Across these four scenarios, we implemented six AP models, ranging from the baseline with no APs used (No APs) and conventional APs provided by the BINGO software (BINGO), to the four proposed WAP variants (ADB4, BL4, LADB4, and Meyer).

Figure 2 illustrates the geometric network design, including the spatial distribution of GCPs and CHKs, as well as the camera exposure stations and associated image coverage. Figure 2a displays the layout shared by Types 1 and 2 (low-density configuration), while Figure 2b presents that for Types 3 and 4 (high-density configuration).

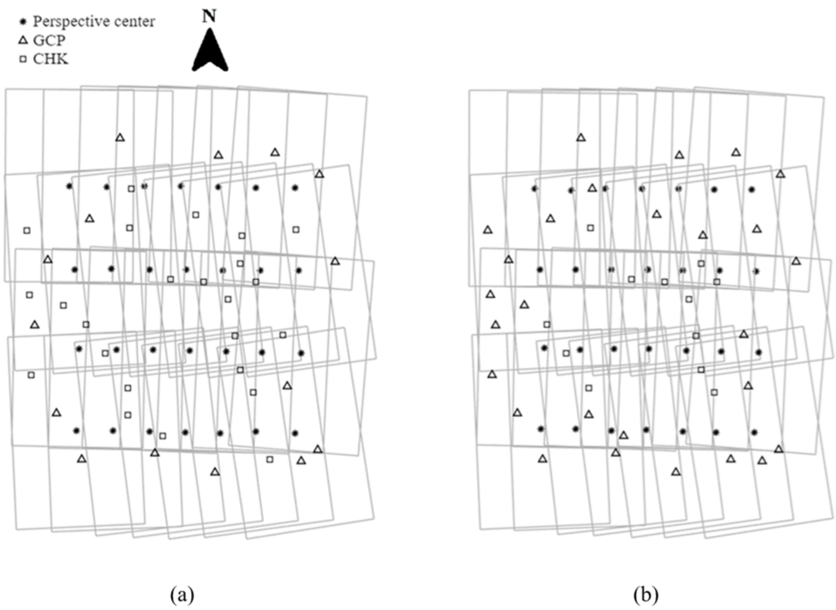

Figure 2. Spatial distribution of GCPs, CHKs, camera exposure stations, and image coverage for the empirical tests: (a) Types 1 and 2; (b) Types 3 and 4.

4. RESULTS AND ANALYSIS

The image-coordinate outlier detection and removal procedure described in Section 3 eliminated blunder observations during the bundle adjustment. As a result, the actual numbers of valid GCPs and CHKs utilized across all test cases varied slightly from their initial nominal configurations, as detailed in Table 1. Furthermore, after outlier detection and removal, the average redundancy across all test cases consistently ranged from 0.43 to 0.50, thereby providing a robust reliability for the adjustment network. The geometric distribution of these control points affected the average intersection ray counts for both GCPs and CHKs. Specifically, under the sparse control configuration (Types 1 and 2), the average ray counts were 2.0–3.6 for GCPs and 5.0–6.6 for CHKs. In contrast, these values increased to 2.0–4.3 and 7.3–8.6, respectively, under the dense control configuration (Types 3 and 4).

Table 1. Exact numbers of utilized GCPs/CHKs across all cases.

	No APs	BINGO	ADB4	BL4	LADB4	Meyer
Type 1	15/24	12/23	13/24	12/23	12/23	13/23
Type 2	15/24	15/23	12/23	13/23	12/23	12/23
Type 3	27/12	27/12	24/12	22/12	24/12	24/12
Type 4	27/12	27/12	27/12	23/12	26/12	25/12

Figure 3 presents the external accuracy, expressed as the root-mean-square differences (RMSDs) at all CHKs across all test cases, for both the horizontal (Figure 3a) and vertical (Figure 3b) components. Overall, incorporating APs substantially improves object-space accuracy across all scenarios, yielding RMSD(XY) and RMSD(Z) reductions of 78.8%–86.3% and 77.8%–97.9%, respectively, compared with the uncompensated cases. The external accuracy improves consistently as control configurations become better. However, increasing the density of peripheral GCPs has a more pronounced effect on increasing accuracy than integrating GNSS/IMU data. For the developed methods, shifting from Type 1 to Type 3 (densifying GCPs alone) reduces the RMSD(XY) by 23.9%–40.1% and the RMSD(Z) by 33.6%–73.1%. In contrast, transitioning from Type 1 to Type 2 (incorporating GNSS/IMU alone) yields improvements of 7.0%–12.1% in RMSD(XY) and 3.7%–40.1% in RMSD(Z). Under the sparsest control configuration (Type 1), the Meyer model achieves an RMSD(XY) of 1.72 GSD; in contrast, the BL4 model delivers the optimal RMSD(XY) of 1.19 GSD under the densest control configuration (Type 4). These trends indicate that both traditional APs and the developed WAP models are effective at mitigating systematic distortions within the horizontal block geometry. Notably, all four developed WAP models significantly outperform BINGO in RMSD(Z) under the Type 1 configuration, with the LADB4 model achieving a 77.4% improvement. Furthermore, all AP models converge toward an optimal RMSD(Z) range of 1.18–2.73 GSD as geometric constraints strengthen with higher GCP densities (Types 3 and 4). A localized exception occurs in Type 2, where BINGO yields an RMSD(Z) of 1.67 GSD, outperforming the developed WAP models, which range from 3.54 to 4.50 GSD. In these WAP cases, the complete rejection of photo-coordinate observations for two to three peripheral GCPs, the remaining counts of which are listed in Table 1, weakens the geometric rigidity of the network boundary, thereby compromising the overall RMSD(Z).

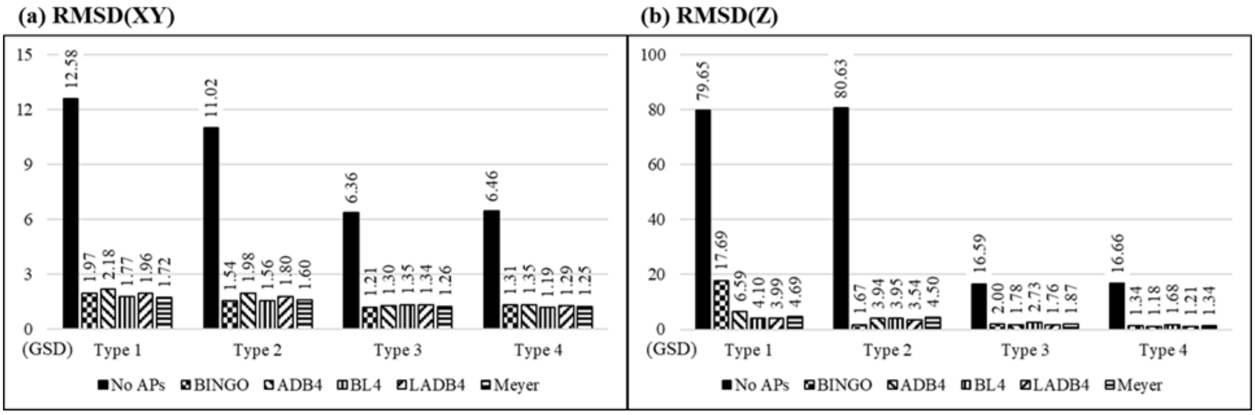

Figure 3. External accuracy across all cases: (a) RMSD(XY), and (b) RMSD(Z).

Figures 4 and 5 demonstrate the internal precision assessment of the bundle adjustment results across all test cases. Figure 4 presents the horizontal and vertical RMS values of tie-point *a posteriori* precisions, denoted as RMS($\hat{\sigma}_{XY}$) and RMS($\hat{\sigma}_{Z}$). Figure 5 illustrates the corresponding *a posteriori* standard deviations of unit weight ($\hat{\sigma}_0$). In contrast to the exception observed in external accuracy, the internal precision metrics show highly consistent and superior performance for the developed WAP models across all four scenarios. In terms of RMS($\hat{\sigma}_{XY}$), all developed WAP models outperform BINGO across all configurations, achieving an RMS range of 0.50–0.88 GSD compared to 1.07–1.15 GSD for BINGO. Regarding RMS($\hat{\sigma}_{Z}$), the ADB4 model under the Type 1 configuration achieves an RMS of 0.89 GSD, representing a 61.7% improvement over BINGO. Crucially, in the Type 2 scenario where BINGO previously exhibited favorable external accuracy, Figure 4 reveals an internal geometric weakness: BINGO exhibits an RMS($\hat{\sigma}_{Z}$) of 1.95 GSD, whereas all four developed WAP models maintain a superior range of 1.25–1.35 GSD, representing a 30.7%–36.0% improvement over BINGO. The $\hat{\sigma}_0$ values in Figure 5 confirm this trend: while incorporating APs inherently reduces $\hat{\sigma}_0$, the developed WAP models achieve a more pronounced reduction, consistently yielding lower values than BINGO across all scenarios. Furthermore, a slight upward trend in $\hat{\sigma}_0$ is observed across all models as the density of GCPs increases. This trend reflects the effects of data filtering. Sparse control configurations impose weaker geometric constraints, eliminating more image observations during outlier detection and removal, leaving a filtered subset of points with better quality. Conversely, denser configurations allow the system to retain more valid observations, introducing random observational variations into the final adjustment.

To resolve the geometric inconsistency in which BINGO exhibits favorable external accuracy but degraded internal precision metrics under the Type 2 scenario, this study selects the Type 2 configuration as the representative scenario for subsequent distortion vector and residual analyses. Figure 6 displays the estimated camera distortion vectors derived from the AP models for both the BINGO and BL4 cases under this specific constraint. The mathematical properties of polynomial APs and WAPs fundamentally dictate their respective compensation mechanisms within the bundle adjustment. Unlike the global polynomial APs in BINGO, which lack spatial adaptability, the developed WAPs offer spatial localization capabilities. Despite these underlying methodological differences, the distortion vectors in Figure 6 reveal a globally similar, symmetric radial distortion pattern. This overall resemblance shows that the dominant systematic distortion trends mask the localized geometric variations between the two formulations. Therefore, a more rigorous evaluation requires an investigation of the image-coordinate residual vectors.

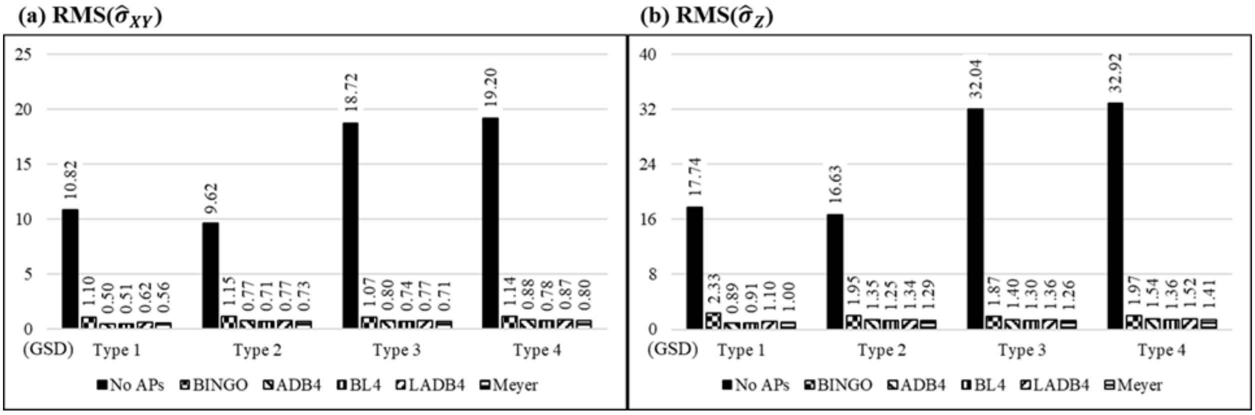

Figure 4. RMS values of tie-point *a posteriori* precisions across all cases: (a) RMS($\hat{\sigma}_{XY}$), and (b) RMS($\hat{\sigma}_{Z}$).

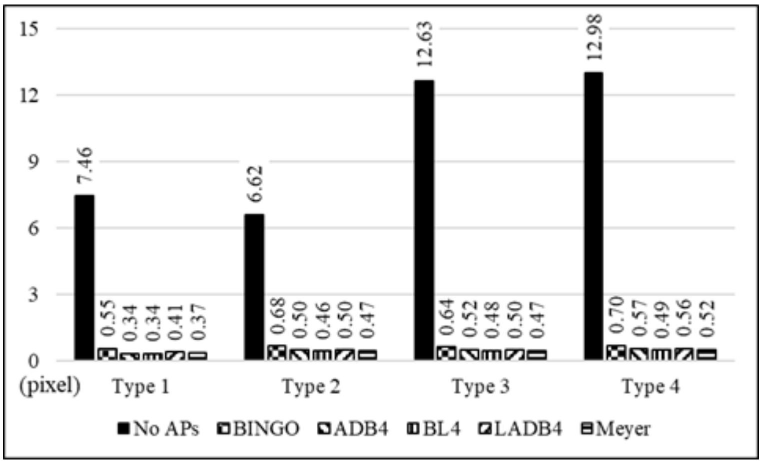

Figure 5. $\hat{\sigma}_0$ across all cases

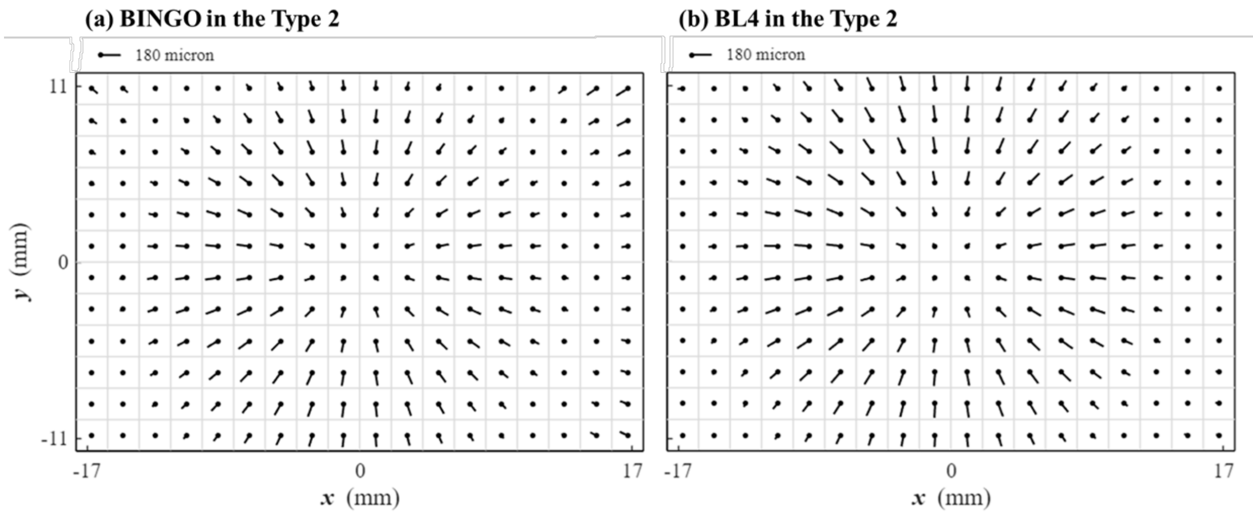

Figure 6. Estimated camera distortion vectors under the Type 2 configuration: (a) BINGO model, and (b) BL4 model.

The grid-based average residual vectors for all photo-coordinate observations, illustrated in Figure 7, further reflect the compensation efficiency of these two approaches. Specifically, the BINGO case retains pronounced systematic residual patterns, whereas the BL4 model eliminates these systematic trends at the same 6 µm scale. Figure 8 illustrates the histograms of the image-coordinate residuals v_x and v_y, using the $\hat{\sigma}_0$ values from the BINGO and BL4 cases as the bin width. The histograms exhibit a truncated leptokurtic distribution, with 83.2%–86.3% of the residuals enclosed within $\pm\hat{\sigma}_0$. Notably, the BL4 model demonstrates a more symmetric distribution than the BINGO model, particularly in the v_y component. Although the WAPs involve a larger parameter set, the applied statistical screening workflow effectively eliminates redundant terms.

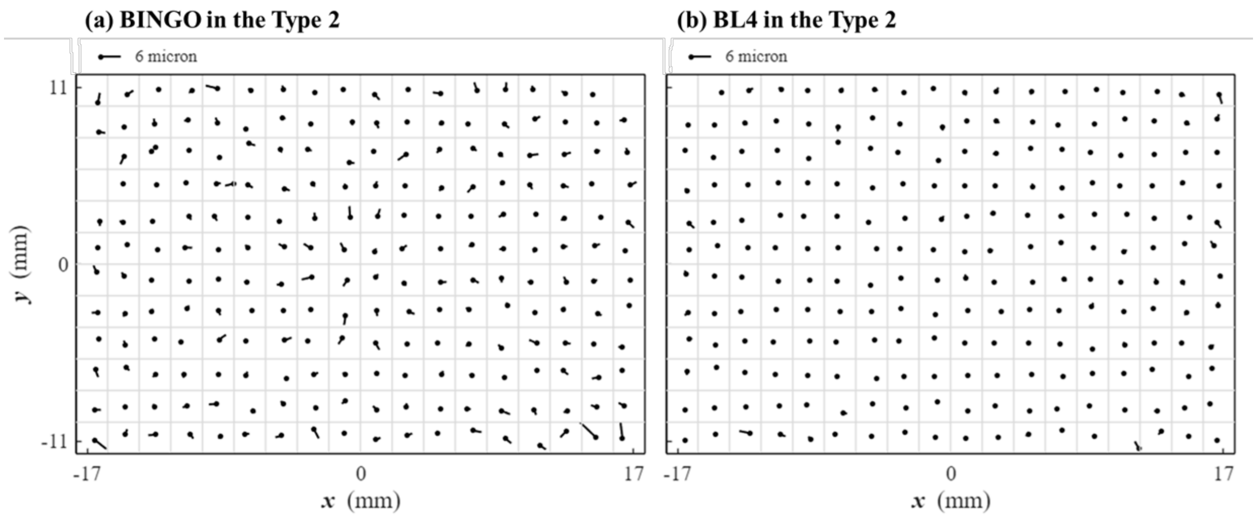

Figure 7. Average image-coordinate residual vectors under the Type 2 configuration: (a) BINGO model, and (b) BL4 model.

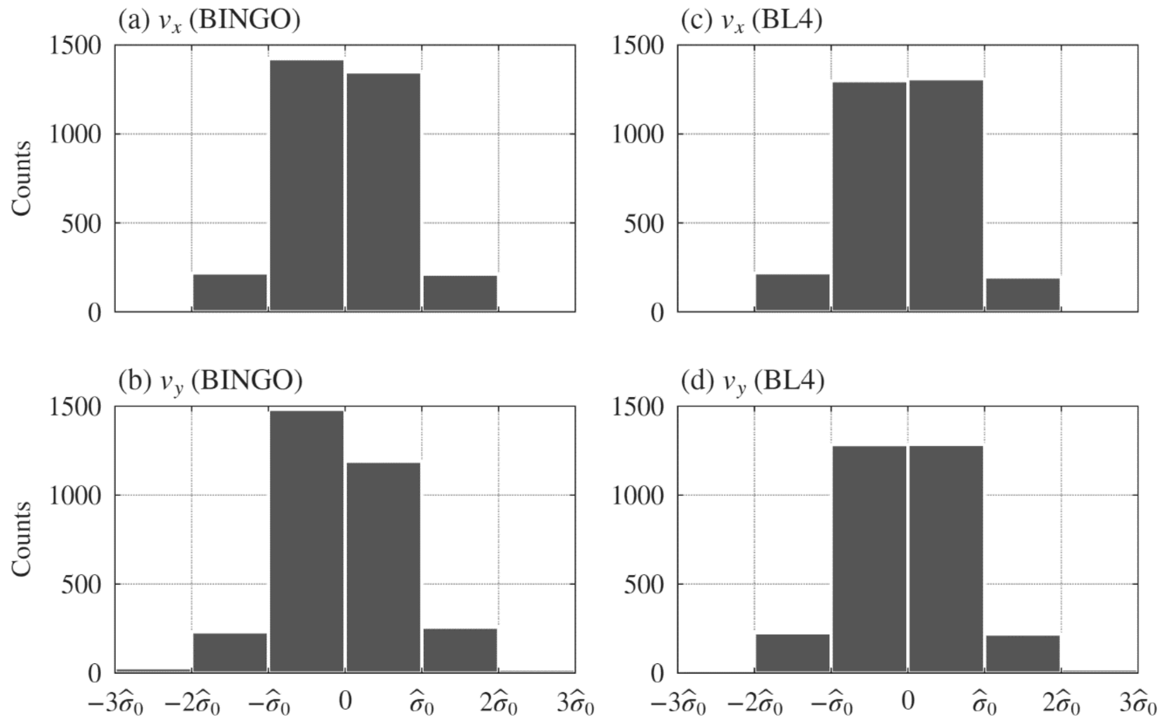

Figure 8. Histograms of the image-coordinate residuals v_x and v_y under the Type 2 configuration for BINGO and BL4 models, respectively.

Table 2 lists the initial and significant number of APs for each model across all configurations. Table 3 further details the adaptive ranges of the translation parameters in Equation (11), highlighting the spatial localization of the wavelet bases. This combination of parameter reduction and adaptive translation prevents over-parameterization during the bundle adjustment. Furthermore, Table 4 summarizes the maximum absolute values of correlation coefficients among the estimated parameters across all scenarios. Notably, the correlation statistics for BINGO remain incomplete because the software reports only the correlation coefficients between the APs and the interior orientation parameters (IOPs). Nevertheless, the available correlation statistics confirm that the wavelet bases' orthogonality effectively suppresses correlations, ensuring a numerically stable adjustment system even in the sparsest control configuration. Consequently, this statistically and numerically rigorous model structure directly improves the final positioning accuracy in object space.

Table 2. Number of significant/initial APs across all cases.

	BINGO	**ADB4**	**BL4**	**LADB4**	**Meyer**
Type 1	18 / 32	222 / 260	182 / 240	151 / 234	202 / 330
Type 2	17 / 32	222 / 308	170 / 220	153 / 252	191 / 300
Type 3	15 / 32	206 / 260	178 / 220	158 / 252	192 / 300
Type 4	17 / 32	206 / 260	176 / 220	152 / 240	187 / 280

Table 3. Adaptive ranges of the translation parameters in Equation 11.

	Translation parameters	ADB4	BL4	LADB4	Meyer
Type 1	k_x	-4 ~ +8	-5 ~ +6	-3 ~ +9	-6 ~ +8
	k_y	-2 ~ +7	-4 ~ +5	+0 ~ +8	-4 ~ +6
Type 2	k_x	-4 ~ +9	-5 ~ +5	-3 ~ +10	-7 ~ +7
	k_y	-2 ~ +8	-4 ~ +5	+0 ~ +8	-4 ~ +5
Type 3	k_x	-4 ~ +8	-5 ~ +5	-3 ~ +10	-6 ~ +8
	k_y	-2 ~ +7	-4 ~ +5	+0 ~ +8	-4 ~ +5
Type 4	k_x	-4 ~ +8	-5 ~ +5	-1 ~ +10	-6 ~ +7
	k_y	-2 ~ +7	-4 ~ +5	+0 ~ +9	-4 ~ +5

Table 4. Maximum absolute values of correlation coefficients in the correlation analysis.

	AP Type	IOPs	Intra-APs	EOPs	GNSS Shift/Drift	IMU Shift/Drift
Type 1	BINGO	0.75	0.77	N/A	-	-
	ADB4	< 0.01	< 0.01	0.03	-	-
	BL4	< 0.01	< 0.01	< 0.01	-	-
	LADB4	< 0.01	< 0.01	< 0.01	-	-
	Meyer	< 0.01	< 0.01	< 0.01	-	-
Type 2	BINGO	0.73	0.70	N/A	N/A	N/A
	ADB4	< 0.01	< 0.01	< 0.01	< 0.01	< 0.01
	BL4	< 0.01	< 0.01	< 0.01	< 0.01	< 0.01
	LADB4	< 0.01	< 0.01	< 0.01	< 0.01	< 0.01
	Meyer	< 0.01	< 0.01	< 0.01	< 0.01	< 0.01
Type 3	BINGO	0.73	0.67	N/A	-	-
	ADB4	< 0.01	< 0.01	0.03	-	-
	BL4	< 0.01	< 0.01	< 0.01	-	-
	LADB4	< 0.01	< 0.01	< 0.01	-	-
	Meyer	< 0.01	< 0.01	< 0.01	-	-
Type 4	BINGO	0.74	0.69	N/A	N/A	N/A
	ADB4	< 0.01	< 0.01	< 0.01	< 0.01	< 0.01
	BL4	< 0.01	< 0.01	< 0.01	< 0.01	< 0.01
	LADB4	< 0.01	< 0.01	< 0.01	< 0.01	< 0.01
	Meyer	< 0.01	< 0.01	< 0.01	< 0.01	< 0.01

5. CONCLUSIONS

This study evaluated the effectiveness of the developed WAP models for non-metric camera self-calibration under diverse control and navigation constraints. Based on the empirical findings from the 24 test cases, the following critical conclusions are drawn:

The WAP models demonstrate exceptional capability to strengthen horizontal and vertical block geometries, yielding RMSD(XY) and RMSD(Z) reductions of 78.8%–86.3% and 83.6%–95.6%, respectively, relative to the uncompensated cases. Unlike global polynomial models that suffer from underfitting, WAPs successfully mitigate both stationary and non-stationary lens distortions in non-metric camera systems.

Under the Type 2 configuration (sparse GCPs supplemented with navigation data), the traditional BINGO polynomial model exhibits favorable external accuracy but degraded internal precision metrics. In contrast, the WAP models outperform the BINGO model by 33.3%–38.4% and 30.7%–36.0% in the RMS($\hat{\sigma}_{XY}$) and RMS($\hat{\sigma}_{Z}$) of tie-point *a posteriori* precisions, respectively. Ultimately, the WAP models sustain this superior internal geometric consistency while minimizing $\hat{\sigma}_0$ values robustly across all configurations.

Combining an adaptive translation-parameter scheme with a rigorous statistical screening workflow enables the developed models to prevent overparameterization. Furthermore, the mathematical orthogonality of the wavelet bases suppresses correlations among estimated parameters, thereby ensuring high numerical stability in the adjustment system, even under the sparsest geometric constraints.

In summary, the WAP models provide a mathematically rigorous, spatially adaptive, numerically stable, and superior alternative to traditional polynomial self-calibration. This approach effectively bridges the gap between low-cost, non-metric imaging sensors and high-precision photogrammetric mapping, unlocking significant potential for UAV-based remote sensing and aerial surveying.

ACKNOWLEDGMENTS

We sincerely appreciate the National Science and Technology Council (NSTC), Taiwan, for the financial support for our research projects for seven years with the following research grants: MOST 105-2119-M-006-032, MOST 106-2119-M-006-023, MOST 107-2119-M-006-019, MOST 108-2621-M-006-002, MOST 109-2121-M-006-002, MOST 110-2121-M-006-004, and MOST 111-2121-M-006-011.

REFERENCES

Ackermann, F. 1981. "Block Adjustment with Additional Parameters." *Photogrammetria* 36 (6): 217–27. https://doi.org/10.1016/0031-8663(81)90040-5

Baarda, W. 1968. A Testing Procedure for Use in Geodetic Networks. Netherlands Geodetic Commission. https://doi.org/10.54419/t8w4sg

Brown, D. C. 1968. Advanced Methods for the Calibration of Metric Cameras. Final Report, Part 1. DBA Systems, Inc. https://apps.dtic.mil/sti/pdfs/AD0706870.pdf

Brown, D. C. 1971. "Close-Range Camera Calibration." *Photogrammetric Engineering* 37 (8): 855–66.

http://vigir.missouri.edu/Images/Caltech-Toolbox/papers/Brown71.pdf

Brown, D. C. 1976. "The Bundle Adjustment—Progress and Prospects." Invited paper, Commission III, No. 03. *International Archives of Photogrammetry* 21 (3): 1–33. https://goobi.tib.eu/viewer/image/1066535345/502/LOG_0056/

Clarke, T. A., and J. G. Fryer. 1998. "The Development of Camera Calibration Methods and Models." *Photogrammetric Record* 16 (91): 51–66. https://doi.org/10.1111/0031-868X.00113

Conrady, A. E. 1919. "Decentred Lens-Systems." *Monthly Notices of the Royal Astronomical Society* 79 (5): 384–90. https://doi.org/10.1093/mnras/79.5.384

Cramer, M. 2009. Digital Camera Calibration. EuroSDR Official Publication No. 55. EuroSDR. http://www.eurosdr.net/sites/default/files/uploaded_files/eurosdr_publication_ndeg_55.pdf

Daubechies, I. 1992. Ten Lectures on Wavelets. *SIAM*. https://doi.org/10.1137/1.9781611970104

Ebner, H. 1976. "Self Calibrating Block Adjustment." Invited paper, Commission III, No. 04. *International Archives of Photogrammetry* 21 (3): 1–17. https://goobi.tib.eu/viewer/image/1066535345/540/LOG_0057/

Fraser, C. S. 1982. "Film Unflatness Effects in Analytical Non-Metric Photogrammetry." *International Archives of Photogrammetry and Remote Sensing* 24 (5): 156–66. https://goobi.tib.eu/viewer/image/1066783985/171/LOG_0028/

Fraser, C. S. 1997. "Digital Camera Self-Calibration." *ISPRS Journal of Photogrammetry and Remote Sensing* 52 (4): 149–59. https://doi.org/10.1016/S0924-2716(97)00005-1

Fritsch, D. 2015. "Some Stuttgart Highlights of Photogrammetry and Remote Sensing." In *Photogrammetric Week 2015*: 3–20. https://phowo.ifp.uni-stuttgart.de/publications/phowo15/010Fritsch.pdf

Fritsch, D. 2017. "Photogrammetrische Auswertung digitaler Bilder – Neue Methoden der Kamerakalibration, dichten Bildzuordnung und Interpretation von Punktwolken." In *Photogrammetrie und Fernerkundung*, edited by Christian Heipke, 157–96. Springer Spektrum. https://doi.org/10.1007/978-3-662-47094-7

Grün, A. 1978. "Progress in Photogrammetric Point Determination by Compensation of Systematic Errors and Detection of Gross Errors." Nachrichten aus dem Karten- und Vermessungswesen 22: 113–40. https://www.researchgate.net/publication/259705209

Kruck, E. J. 2021. *BINGO 7.4 User's Manual*. GIP.

Laussedat, A. 1898. Recherches sur les instruments, les méthodes et le dessin topographiques. Vol. 1, *Aperçu historique sur les instruments et les méthodes*. Gauthier-Villars. https://archive.org/details/b2487789x_0001/

Magill, A. A. 1955. "Variation in Distortion with Magnification." *Journal of Research of the National Bureau of Standards* 54 (3): 135–42. https://nvlpubs.nist.gov/nistpubs/jres/54/jresv54n3p135_A1b.pdf

Mallat, S. G. 1989. "A Theory for Multiresolution Signal Decomposition: The Wavelet Representation." *IEEE Transactions on Pattern Analysis and Machine Intelligence* 11(7): 674–93. https://doi.org/10.1109/34.192463

Merchant, D. C. 1972. *Metric Calibration of the Aerial Photographic System by the Method of Mixed Ranges*. Department of Geodetic Science Report No. 173. The Ohio State University Research Foundation. https://kb.osu.edu/server/api/core/bitstreams/5e04a124-74da-4051-a195-ceccabb848b4/content

Mikhail, E. M., and F. Ackermann. 1976. *Observations and Least Squares*. IEP.

National Land Surveying and Mapping Center, Ministry of the Interior. 2015. *2015 Annual Project for the Expansion of Airborne Remote Sensing Sensor System Calibration Operations (General Report)*. https://ws.moi.gov.tw/Download.ashx?u=LzAwMS9VcGxvYWQvT2xkRmlsZV9OTFNDL3VwbG9hZGZpbGUvNTk0MTUyLnBkZg%3d%3d&n=NTk0MTUyLnBkZg%3d%3d&icon=..pdf

Tang, R., D. Fritsch, M. Cramer, and W. Schneider. 2012a. "A Flexible Mathematical Method for Camera Calibration in Digital Aerial Photogrammetry." *Photogrammetric Engineering & Remote Sensing* 78 (10): 1069–77. https://doi.org/10.14358/PERS.78.10.1069

Tang, R., D. Fritsch, and M. Cramer. 2012b. "New Rigorous and Flexible Fourier Self-Calibration Models for Airborne Camera Calibration." *ISPRS Journal of Photogrammetry and Remote Sensing* 71: 76–85. https://doi.org/10.1016/j.isprsjprs.2012.05.004

Wolf, P. R., B. A. Dewitt, and B. E. Wilkinson. 2014. *Elements of Photogrammetry with Applications in GIS*. 4th ed. McGraw-Hill Education. https://www.accessengineeringlibrary.com/content/book/9780071761123

Ye, J.-F., J.-R. Tsay, and D. Fritsch. 2024. "Wavelets for Self-Calibration of Aerial Metric Camera Systems." *Photogrammetric Engineering & Remote Sensing* 90 (9): 575–87. https://doi.org/10.14358/PERS.24-00002R2